RSC Advances

PAPER

View Article Online
View Journal | View Issue

Open Access Article. Published on 15 March 2019. Downloaded on 11/6/2025 12:59:15 AM.
This article is licensed under a Creative Commons Attribution-NonCommercial 3.0 Unported Licence.

Check for updates

Cite this: *RSC Adv.*, 2019, **9**, 8684

Preparation of Ni based mesoporous Al_2O_3 catalyst with enhanced CO_2 methanation performance†

Jianghui Lin,‡[a] Caiping Ma,‡[bc] Jing Luo,[d] Xianghui Kong,[a] Yanfei Xu,[a] Guangyuan Ma,[a] Jie Wang,[a] Chenghua Zhang,*[e] Zhengfeng Li[a] and Mingyue Ding*[af]

A Ni based mesoporous γ-Al_2O_3 (MA) catalyst was prepared *via* partial hydrolysis without organic surfactants and employed in the carbon dioxide methanation reaction. The obtained catalysts were characterized by N_2 adsorption–desorption, H_2-TPR, XRD, XPS, TG, SEM and TEM-EDS techniques. CO_2 methanation was performed in a fixed-bed reactor. A high surface area of MA with excellent hydrothermal stability was obtained, which promoted the dispersion of nickel species, producing a better catalytic performance. Incorporation of more NiO species into the Ni/MA catalyst increased the amount of active metallic Ni sties, further improving the catalytic activity and CH_4 selectivity. Moreover, the monolithic skeleton of MA with fabric-like walls suppressed the aggregation of active metallic Ni sites and carbon deposition, enhancing the catalyst's stability, which provides a new insight for potential industrial applications.

Received 17th December 2018
Accepted 26th February 2019

DOI: 10.1039/c8ra10348h

rsc.li/rsc-advances

1 Introduction

Synthetic natural gas (SNG), as an efficient and clean energy carrier, has the advantages of high combustion efficiency and using existing gas pipelines, attracting more and more attention with the depletion of natural gas and rapid rising of natural gas prices.[1,2] The emission of carbon dioxide into the atmosphere is considered as the major cause of global warming. Many methods including CO_2 capture, separation, storage and converting CO_2 into useful compounds *etc.* have been used to reduce CO_2 emissions, in which the CO_2 methanation reaction ($CO_2 + H_2 \rightarrow CH_4 + H_2O$, $\Delta G = -113$ kJ mol^{-1}) as an efficient approach for converting CO_2 directly to SNG has drawn increasing interest.[3]

In recent years, numerous studies on CO_2 methanation have been carried out for metal-based catalysts with enhanced catalytic activity and stability.[4–6] Many group VIIIB metals such as Fe, Ru, Rh, Ni, Co, *etc.* are used widely, in which Ru and Rh-based catalysts have been reported as the most effective catalysts for CO_2 methanation, whereas higher cost and limited availability restrict their applications.[7] Due to relatively high methanation activity and low price, Ni based catalysts are utilized extensively in the CO_2 methanation process,[8–10] but they are easily suffered from the deactivation due to carbon deposition and nickel sintering compared to noble metal catalysts.[11,12] Low temperature is in favor of CO_2 conversion and the formation of CH_4 according to thermodynamic equilibrium that methanation reaction is an eight-electron process with kinetic barrier.[13] However, complete conversion of CO_2 into CH_4 at low temperature for Ni based catalysts is very difficult from kinetics.[14] It is necessary to modify the Ni-based catalyst for promoting its CO_2 methanation performance.

Promotors (such as MgO, CaO, La_2O_3 and so on),[15–17] supports (including SiO_2, Al_2O_3, ZrO_2 and CeO_2) and reaction conditions (temperature, pressure, space velocity and so on) are extensively adopted to optimize Ni-based catalysts, which play an important role in improving the performance for CO_2 methanation.[18–21] Especially, the nature of the support has a significant influence on the dispersion of active metallic sites and interaction of metal–support.[8] CeO_2 (ref. 22) and/or TiO_2 (ref. 23) supported Ni based catalysts display excellent CO_2 methanation activity and CH_4 selectivity by providing oxide vacancies and enhancing H_2 adsorption, whereas active Ni nanoparticles undergo easily the thermal sintering due to their low Tammann temperature and "hot spots" existed inside the catalyst bed. In addition, mesoporous molecular sieves possessing large surface area and ordered mesoporous channel

[a]School of Power and Mechanical Engineering, Hubei International Scientific and Technological Cooperation Base of Sustainable Resource and Energy, Wuhan University, Wuhan 430072, China. E-mail: dingmy@whu.edu.cn; zhangchh@sxicc.ac.cn

[b]State Key Laboratory of Coal Conversion, Institute of Coal Chemistry, Chinese Academy of Sciences, Taiyuan 030001, China

[c]University of Chinese Academy of Sciences, Beijing 100049, China

[d]Xiamen Tobacco Industrial Co., Ltd., Xiamen 361022, China

[e]Synfuels China Co. Ltd., Beijing 101407, China

[f]Key Laboratory of Advanced Energy Materials Chemistry, Ministry of Education, Nankai University, Tianjin 300071, China

† Electronic supplementary information (ESI) available. See DOI: 10.1039/c8ra10348h

‡ These authors contributed equally to this work.

This journal is © The Royal Society of Chemistry 2019

Open Access Article. Published on 15 March 2019. Downloaded on 11/6/2025 12:59:15 AM.
This article is licensed under a Creative Commons Attribution-NonCommercial 3.0 Unported Licence.

have been developed widely to optimize CO_2 methanation performance.[24–26] However, the silica based zeolites occur easily the collapse of mesoporous structures because of their intrinsic nature of the hydrothermal instability. As a result, designing mesoporous materials with high dispersion of Ni nanoparticles and excellent thermal stability is necessary for CO_2 methanation.

Mesoporous alumina with large surface area and good thermal stability is used as a potential support.[27] The sol–gel method is applied for the preparation of porous alumina, which results easily in the formation of inhomogeneous porous structure *via* the cracking of gels.[28] Xu *et al.*[29] developed a one-step evaporation induced self-assembly (EISA) strategy to synthesize the ordered mesoporous alumina material, which presented the strong metal–support interaction and outstanding thermal stability compared to the traditional non-mesoporous Al_2O_3 support, displaying better catalytic performance. However, low-temperature CO_2 methanation performance is still needed to be improved. Developing a novel and economic stable mesoporous alumina with large surface area and narrow pore size distribution increasingly draws attention. Recently, Shang *et al.*[30] prepared a new mesoporous γ-alumina (MA) material by partial hydrolysis without the adding of organic surfactants, which showed a high surface area and excellent thermal stability up to 900 °C. However, an application of this kind of MA supported Ni based catalyst to CO_2 methanation has never been reported so far.

Herein, we prepared a Ni based catalyst supported on mesoporous γ-alumina synthesized by partial hydrolysis of a nontoxic and inexpensive inorganic aluminum salt. The nickel species loading, interaction of Ni–MA, and CO_2 methanation performance were studied in details. The catalysts were characterized by N_2 physisorption, scanning electron microscopy (SEM), transmission electron microscopy (TEM), X-ray photoelectron spectroscopy (XPS), powder X-ray diffraction (XRD), hydrogen temperature-programmed reduction (H_2-TPR) and thermogravimetric analysis (TG) for obtaining the structure–performance relationship.

2 Experimental

2.1 Catalyst synthesis

MA was prepared *via* a one-pot template-free partial hydrolysis path, as presented in the article.[30] Typically, 0.1 mol of $Al(NO_3)_3 \cdot 9H_2O$ was dissolved in 50 mL of deionized water at 75 °C, and 1 mol L^{-1} $(NH_4)_2CO_3$ aqueous solution was dropped slowly under vigorous magnetic stirring until the formation of transparent gel. The gel was aged for 24 h, and then dispersed in a watch glass at 100 °C for 12 h. The as-prepared solid was treated at 200 °C in air for 10 h to remove ammonium nitrate, and further calcined at 500 °C for 10 h.

The Ni/MA catalysts with different nickel contents were prepared by impregnation method. A certain amount of $Ni(NO_3)_2 \cdot 6H_2O$ was dissolved in distilled water under the stirring and then the MA support was added into nickel nitrate solution under the stirring for 12 h at room temperature. Afterwards, the suspension was dried at 100 °C for 12 h and calcined at 550 °C for 5 h. In this process, the content (wt%) of Ni was changed from 10 to 25%. The prepared Ni-based catalysts were denoted by *X*Ni/MA, where *X* denotes the content of Ni in weight percentage. In contrast, the commercial alumina (CA) modified Ni catalyst was prepared by the impregnation method. The content of Ni was 25% (wt) in the Ni/CA catalyst, which is denoted to 25Ni/CA.

2.2 Catalyst characterization

N_2 adsorption and desorption isotherms were measured by an automatic physical adsorption analyzer (Micromeritics ASAP2020). The sample was degassed at 150 °C for 3 h to remove physical absorbed water and impurities on the surface before the measurement. The specific surface area was calculated by Brunauer–Emmett–Teller (BET) method and pore size distribution was analyzed by Barrett–Joyner–Halenda (BJH) method.

Powder X-ray diffraction (XRD) was performed with a Bruker AXS-D8 Advance (Germany) diffractometer using Co Kα (γ = 1.78 Å) radiation at 35 kV and 40 mA. XPS spectra of the catalysts were checked by a VG system (MultiLab 2000), using an Al Kα X-ray source (1486.6 eV). The C 1s as a reference signal was adjusted to 284.6 eV.

H_2-TPR measurements were performed in a quartz tube equipped with a thermal conductivity detector (TCD). The samples were pretreated with high purity N_2 at 150 °C and a flow rate of 30 mL min^{-1} for 1.5 h to remove water and other contaminants. The samples were cooled down to room temperature, and then 5% H_2/N_2 was introduced into the system at a flow rate of 30 mL min^{-1}. The TCD signal and sample temperature were recorded while the temperature being ramped to 900 °C at a heating rate of 10 °C min^{-1}.

Scanning electron microscopy (SEM) images were obtained on a QUANTA F250 scanning electron microscope to characterize the surface morphology of the catalysts. Energy dispersive X-ray spectroscopy (EDX) was performed on a GENESIS EDX detector. High resolution transmission electron microscopy (HRTEM) experiments were performed in a Philips CM200 high resolution transmission electronic microscopy with 200 kV accelerating voltage.

The amounts of carbon deposition at the used catalysts were determined by a TGA/DSC analyzer (METTLER TOLEDO). After drying at room temperature, a certain amount of sample was heated to 900 °C in air with a heating rate of 10 °C min^{-1} on an Al_2O_3 crucible.

2.3 Catalyst testing

CO_2 methanation was performed at atmospheric pressure in a vertical continuous-flow fixed-bed reactor (inner diameter of 12 mm and a length of 330 mm). The flow of reaction gases was controlled using mass flow controllers. The actual reaction temperature of the catalyst was monitored using a thermocouple placed in the middle of the tubular reactor. 500 mg of the catalyst mixed with 500 mg quartz sand (40–70 mesh) were placed between two layers of quartz wool. Before the reaction, the catalyst was reduced *in situ* at 500 °C with a heating rate of 2 °C min^{-1} under a flow of H_2 at gas hourly space velocity

Open Access Article. Published on 15 March 2019. Downloaded on 11/6/2025 12:59:15 AM.
This article is licensed under a Creative Commons Attribution-NonCommercial 3.0 Unported Licence.

(GHSV) of 2000 mL g^{-1} h^{-1} for 10 h. Subsequently, the temperature was cooled to 200 °C and the mixtures of H_2 and CO_2 (molar ratio $H_2/CO_2 = 4/1$) were introduced into the reactor at 6000 mL g^{-1} h^{-1} of GHSV. The catalytic tests were carried out at different temperatures, ranging from 200 to 500 °C.

The gas products were analyzed using an on-line gas chromatogram (Fuli 9790II) equipped with a TCD detector using porapak Q and Molecular Sieve 5A packed column. The values of CO_2 conversion (X_{CO_2}) and CH_4 selectivity (S_{CH_4}) were calculated by the following equations:

$$X_{CO_2} = \frac{W_{CO_2,in} - W_{CO_2,out}}{W_{CO_2,in}} \times 100\%$$

$$S_{CH_4} = \frac{W_{CH_4,out}}{W_{CH_4,out} + W_{CO,out}} \times 100\%$$

where $W_{CO_2,in}$ and $W_{CO_2,out}$ are relative volume percentage of CO_2 in the feed and effluent gas, and $W_{CH_4,out}$ and $W_{CO,out}$ are relative volume percentage of CH_4 and CO in the effluent gas, respectively.

3 Results and discussion

3.1 Catalyst characterization

3.1.1 N_2 adsorption analysis. The N_2 adsorption–desorption isotherms and corresponding pore size distribution curves of the MA support and Ni/MA catalysts are shown in Fig. 1a and b, respectively. It is apparent from Fig. 1a that the MA support displays the IV type isotherm with an apparent hysteresis loop according to the IUPAC classification. The type H2 hysteresis loop of the MA support appears in the region of 0.4–0.7 p/p_0, indicating a narrow mesopore size distribution.[31] The mesoporous structures of MA remain unchanged after the adding of NiO species, as shown in Fig. 1a, suggesting that mesoporous structures of MA are not destroyed after adding the Ni species. BJH pore size analysis shown in Fig. 1b presents that all of the Ni/MA catalysts exhibit narrow pore size distribution around 3.5 nm.

Surface area (S_{BET}), pore volume (V_P) and pore diameter (D_P) of the MA support and Ni/MA catalysts with different nickel loadings are presented in Table 1. BET surface area, average pore volume and pore diameter of MA is 237.0 m^2 g^{-1}, 0.32 cm^3 g^{-1} and 3.1 nm, respectively. In contrast, BET surface area of CA is 166.2 m^2 g^{-1}, which is lower than that of MA (237.0 m^2 g^{-1}), demonstrating that preparation of MA by partial hydrolysis of inorganic aluminum salt facilitates the increase of BET surface area compared to the traditional preparation method of CA. As Ni species is added into the MA support, the BET surface area presents a slight decreasing trend. The BET surface area decreases slowly from 158.8 m^2 g^{-1} of 10Ni/MA to 152.4 m^2 g^{-1} of 25Ni/MA. The average pore diameter of Ni/MA catalysts is in the range of 3.3–4.0 nm (Table 1), while the average NiO crystalline diameter calculated by Scherrer equation from XRD is over 10 nm, indicating that Ni species are dispersed mainly on the MA surface without entering into the mesoporous structures of MA. Therefore, it is possible that partial blockage of NiO particles on the surface of MA results in the decrease of BET surface area and pore volume.[32] In addition, with the gradual increasing of Ni species content, the NiO nanoparticles size presents an increasing trend. The crystalline size of NiO increases from 13.6 to 22.7 nm as the Ni content increases from 10 to 25 wt%, implying that the adding of more Ni species facilitates the formation of larger crystallites. On the other hand, the 25Ni/CA catalyst presents 100.3 m^2 g^{-1} of BET surface area, which is only two-thirds of the 25Ni/MA catalyst (152.4 m^2 g^{-1}), whereas the crystallites size (31.7 nm) of Ni species over the 25Ni/CA is 1.4 times bigger than that of 25Ni/MA, revealing better dispersion ability of MA compared to CA.

3.1.2 H_2-TPR results. The reduction behavior of the Ni/MA catalysts with different nickel loadings is analyzed by H_2-TPR in Fig. 2a. It is reported that the reduced Ni species are usually divided into three types (α, β and γ) based on the peak temperature.[33] The α-type NiO is free nickel oxide located in the low temperature (about 420 °C), which has a weak interaction with the Al_2O_3 support. The β-type is assigned to the NiO species

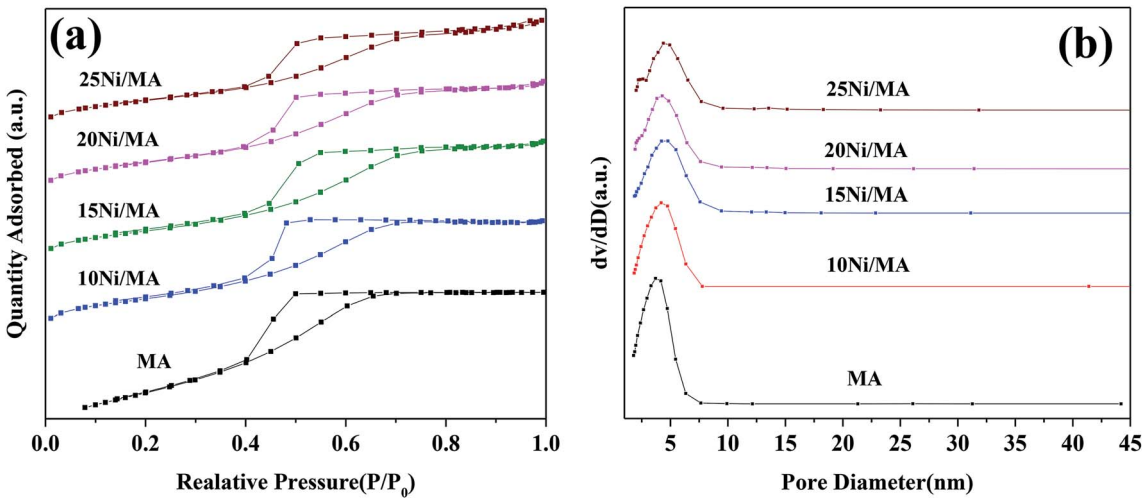

Fig. 1 (a) N_2 adsorption–desorption isotherms and (b) BJH pore size distributions of the support and Ni/MA catalysts.

Open Access Article. Published on 15 March 2019. Downloaded on 11/6/2025 12:59:15 AM.
This article is licensed under a Creative Commons Attribution-NonCommercial 3.0 Unported Licence.

Table 1 Textural properties of the as-prepared catalysts

Sample	S_{BET}[a]/(m^2 g^{-1})	D_p[b]/(nm)	V_p[c]/(cm^3 g^{-1})	Crystalline size[d]/(nm)
CA	166.2	4.69	0.32	—
MA	237.0	3.10	0.25	—
10Ni/MA	158.8	3.36	0.18	13.6
15Ni/MA	156.7	3.81	0.20	15.8
20Ni/MA	156.6	3.74	0.19	17.6
25Ni/MA	152.4	4.00	0.22	22.7
25Ni/CA	100.3	4.97	0.25	31.7

[a] Calculated by the BET equation. [b] BJH desorption average pore diameter. [c] BJH desorption pore volume. [d] Average NiO crystalline diameter calculated by Scherrer equation from XRD.

possessing a middle interaction with the support in the mild-temperature region (about 450–650 °C). The γ-type belongs to the less reducible $NiAl_2O_4$ in the high-temperature region (about 650–850 °C).[34] As shown in Fig. 2a, reduction peaks of nickel species shift slowly towards lower temperature with the increasing in NiO concentration, indicating that the Ni/MA catalyst with higher nickel loading facilitates the reduction of nickel oxide species. As known mentioned above (Table 1), the NiO nanoparticles size increases gradually with the increase in Ni species content. It is possible that a larger NiO particle size in the Ni/MA catalysts weakens the metal–support interaction, promoting the reduction of NiO species.[35] In addition, the

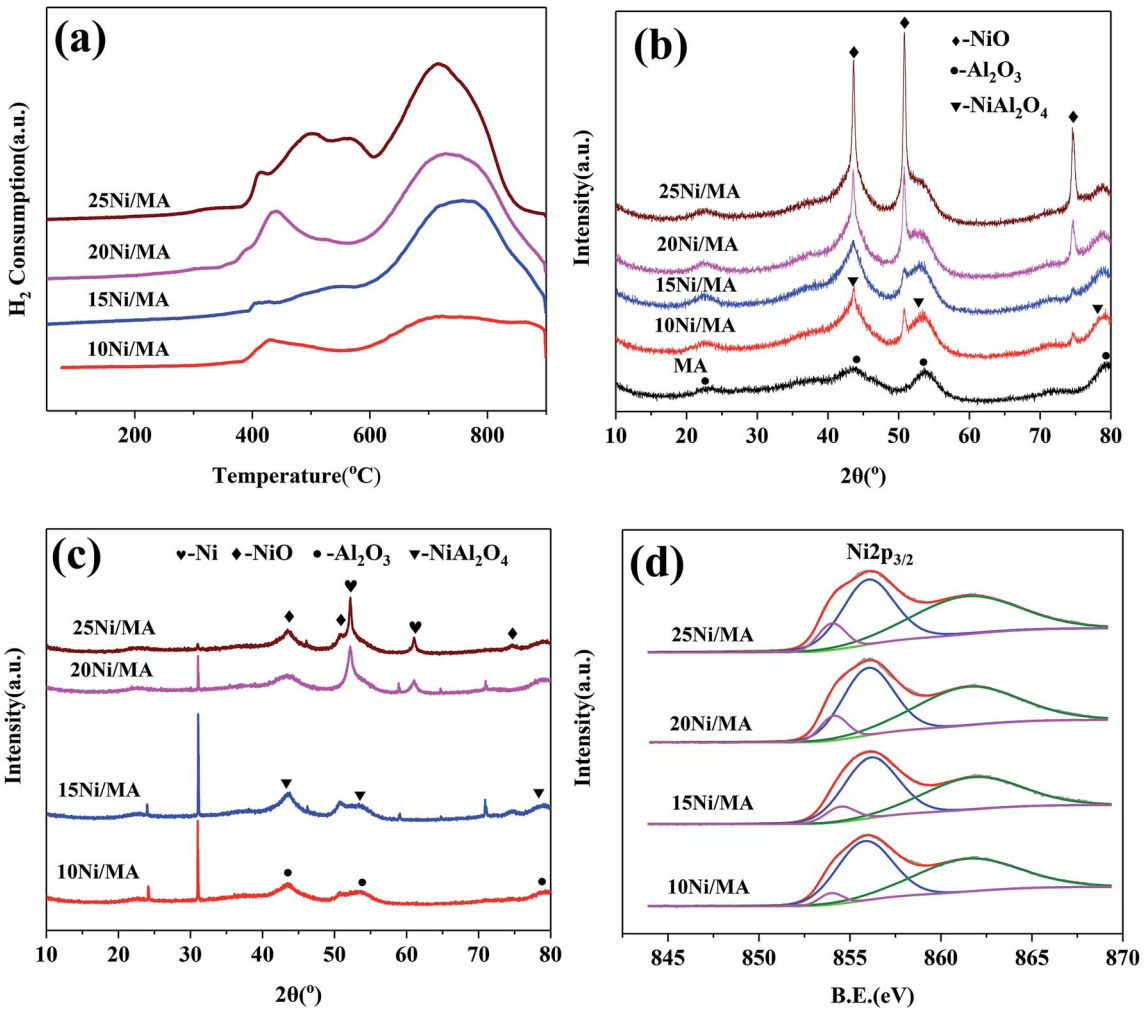

Fig. 2 (a) H_2-TPR profiles of the fresh Ni/MA catalysts, (b) XRD patterns of the fresh Ni/MA catalysts, (c) XRD patterns of the spent Ni/MA catalysts and (d) XPS spectra in Ni 2p of the fresh Ni/MA catalysts.

Open Access Article. Published on 15 March 2019. Downloaded on 11/6/2025 12:59:15 AM.
This article is licensed under a Creative Commons Attribution-NonCommercial 3.0 Unported Licence.

Table 2 XPS calculate data of the fresh Ni/MA catalysts

Sample	S_{NiO}/S_T (%)
10Ni/MA	8.1
15Ni/MA	12.7
20Ni/MA	19.1
25Ni/MA	20.3

intensity of β-type NiO presents an increasing trend with the increasing in nickel loading, implying that incorporation of more NiO species in the Ni/MA catalysts is in favor of the formation of β-type NiO species. Xu *et al.*[29] prepared the mesoporous NiO modified Ni catalyst *via* one-step evaporation induced self-assembly method, which is composed mainly of γ-type $NiAl_2O_4$ with much strong metal–support interaction that hard to be reduced to Ni^0 active site. Therefore, the formation of β-type NiO and α-type NiO in the present study suggests that the MA modified Ni catalyst *via* partial hydrolysis without using organic surfactants decreases the interaction of Ni–Al_2O_3, promoting the reduction of Ni species.

3.1.3 XRD analysis. Fig. 2b shows XRD patterns of the support and fresh Ni/MA catalysts with different nickel contents. It is seen that diffraction peaks at $2\theta = 22.5°$, 43.9°, 53.6°, 79.2° are observed for the support, which are attributed to alumina phase (JCPDS no. 50-0741). Combined with the BET results, it is considered that the MA support is composed mainly of mesoporous γ-Al_2O_3. As nickel species is added into MA, diffraction peaks of NiO phase appear at $2\theta = 43.5°$, 50.7°, 74.5° (JCPDS no. 71-1179). In addition, broad diffraction peaks at $2\theta = 43.3°$, 52.8°, 77.8° (JCPDS no. 10-0339) assigned to $NiAl_2O_4$ are observed in the Ni/MA catalysts. This indicates that incorporation of nickel species into MA results in the formation of NiO and $NiAl_2O_4$, which is consistent with the H_2-TPR results. It is apparent that the intensity of NiO diffraction peaks increases gradually with the increase of Ni content from 10 to 25 wt%, which demonstrates that incorporation of more Ni species into MA promotes the formation of NiO phase.[32] Combined with the BET results, it is considered that the NiO particles are formed mainly on the surface of MA without entering into the pore channel. Besides, the intensity of $NiAl_2O_4$ diffraction peaks presents a slightly decreasing trend with the increasing Ni loading, implying that the Ni loading increasing weakens the interaction of metal–support *via* the increase of particles size of NiO, decreasing the amount of Ni-Al solid solution.

After reaction, new diffraction peaks at $2\theta = 52.2°$, 61.0° appeared in the XRD patterns (shown in Fig. 2c) are assigned to Ni phase (JCPDS no. 87-0712). It is found that the intensity of Ni diffraction peaks presents an increasing trend with the increasing in nickel species content. The highest fraction of metallic Ni phase is observed over the 25Ni/MA catalyst, which confirms the formation of more metallic Ni sites for the Ni/MA catalyst with higher Ni loading. It is accepted that metallic Ni sites play a crucial role in promoting the CO_2 methanation reaction.

3.1.4 XPS analysis. Phase compositions on the surface layers of the Ni/MA catalysts are further analyzed by XPS. As shown in Fig. 2d, a main Ni $2p_{3/2}$ peak around 855.8 eV with a shoulder peak around 862.0 eV have appeared for all of the Ni/MA catalysts, which are attributed to the Ni^{2+} peaks in the form of $NiAl_2O_4$ spinel species,[36] indicating that the $NiAl_2O_4$ species is formed on the surface of the Ni/MA catalysts. In addition, a Ni $2p_{3/2}$ peak around 854.0 eV also exists, corresponding to the NiO species.[37] The intensity of NiO peak on the surface layers presents a slightly increasing trend with the increasing Ni concentration in the Ni/MA catalysts. The ratio of S_{NiO} to S_T ($S_{NiO} + S_{NiAl_2O_4}$) over the Ni/MA catalysts is calculated according to the area integrals of NiO and $NiAl_2O_4$, and listed in Table 2. It can be found that the ratio of S_{NiO} to S_T increases from 8.1 to 20.3% with the increase of Ni loading from 10 to 25 wt%, revealing the formation of more NiO on the catalyst surface with higher nickel contents. The increasing NiO content for the Ni/MA catalyst with higher Ni loading promotes the formation of active metallic Ni sites for CO_2 methanation. This is in agreement with the results of XRD and H_2-TPR.

3.1.5 SEM and TEM results. The morphologies and porous structures of the support and Ni/MA catalysts are characterized by SEM. It can be seen from Fig. 3a that the MA support consists of various types of monolithic skeletons with porous framework, which may be stemmed from the nanoparticles aggregation.

As nickel species are added into MA, the fabric-like walls with inside diameter about 100 nm are displayed on the surface layers (Fig. 3b–e). These porous frameworks are well cross-linked together to form the fabric-like walls. It is possible that the combination of Ni species with MA during the impregnation and calcination processes changes the surface morphologic structures of Ni/MA. NiO spherical particles are observed inside the fabricate walls, and the nanoparticles size increases with the increasing nickel content in the Ni/MA catalysts. After reaction, the fabric-like structures remain almost unchanged (Fig. 3f–i), validating the excellent hydrothermal stability of Ni/MA. There is no particle aggregation of Ni species is during reaction, suggesting that the MA support played an important role in restraining the sintering of Ni particles. In addition, no obvious carbon deposition is observed for the Ni/MA catalyst in the SEM patterns, indicating that the distinct monolithic skeleton of MA facilitates the transfer of reaction and product molecules, and suppresses the carbon deposition on the surface of MA.

TEM measurements are performed to characterize the structure and distribution of Ni species over the 25Ni/MA catalyst (Fig. 4). Two kinds of lattice spacing about 0.24 nm and 0.21 nm are observed on the surface of MA (Fig. 4a and b), corresponding to NiO (111) and (200) crystals, respectively.[38,39] The high-angle annular dark field scanning transmission electron microscopy (HAADF-STEM) imaging and elemental mapping from Fig. 4c–f show the distribution of Ni, Al and O elements, respectively. To the marked nanoparticle (red circle marked in Fig. 4c) anchored outside the MA surface, only Ni and O are present while no Al is observed in the mapping shown in Fig. 4d–f, demonstrating the only presence of NiO nanoparticles

Open Access Article. Published on 15 March 2019. Downloaded on 11/6/2025 12:59:15 AM.
This article is licensed under a Creative Commons Attribution-NonCommercial 3.0 Unported Licence.

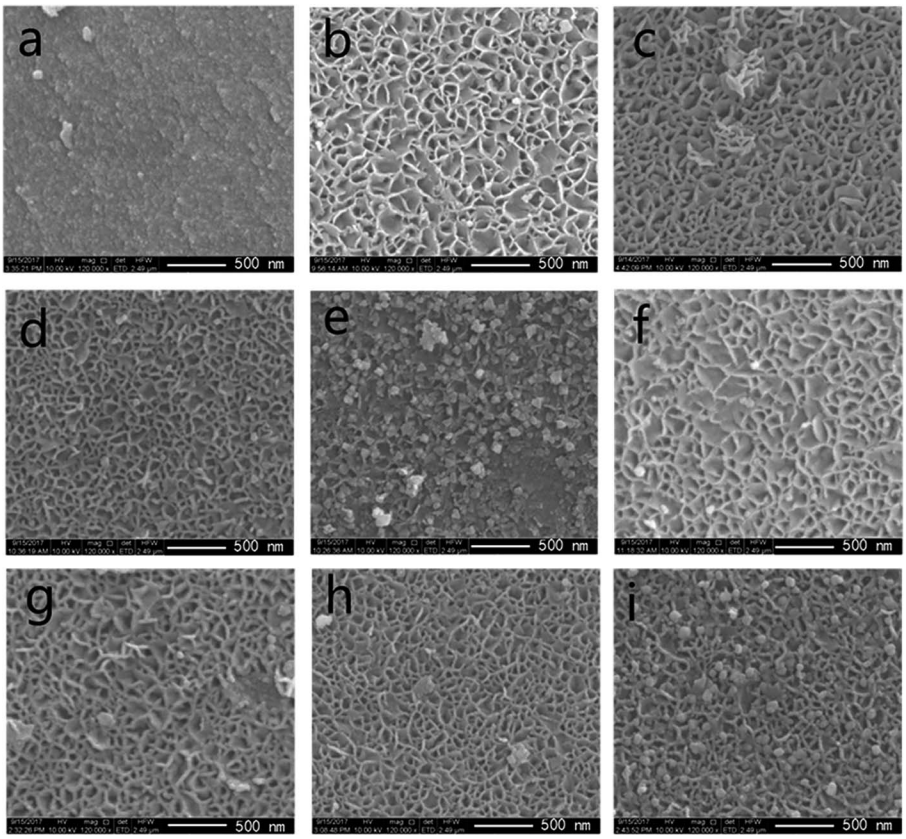

Fig. 3 SEM images of (a) MA support, (b–e) fresh catalysts: 10/15/20/25 Ni/MA and (f–i) spent catalysts: 10/15/20/25 Ni/MA.

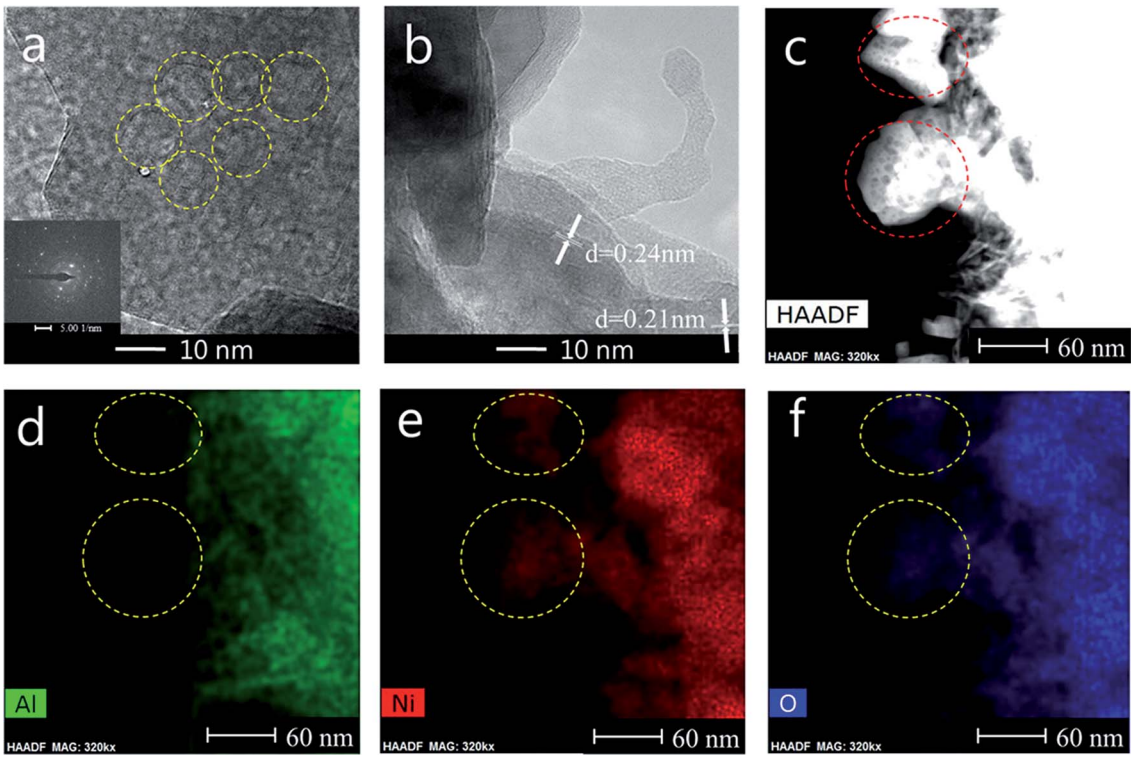

Fig. 4 (a, b) TEM, (c) STEM-HAADF, (d) Al map, (e) Ni map and (f) O map images of the fresh 25Ni/MA catalyst.

Open Access Article. Published on 15 March 2019. Downloaded on 11/6/2025 12:59:15 AM.
This article is licensed under a Creative Commons Attribution-NonCommercial 3.0 Unported Licence.

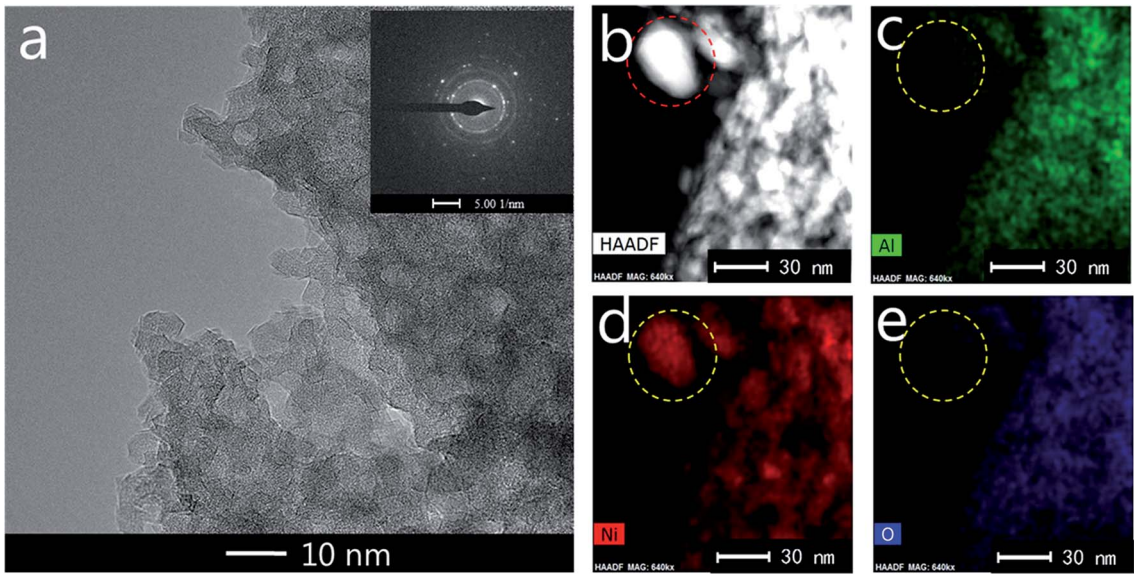

Fig. 5 (a) TEM, (b) STEM-HAADF, (c) Al map, (d) Ni map, (e) O map images of the spent 25Ni/MA catalyst.

on the MA surface. This further validates that Ni species added in the Ni/MA catalysts is mainly covered on the surface layers without entering into the mesoporous structures of MA. The NiO nanoparticle size is about 30 nm, which is comparative with the value calculated by XRD. The combination of TEM, SEM and XRD provides an unambiguous illustration on the NiO particle size distribution of Ni/MA.

TEM images and elemental mapping of the used 25Ni/MA catalyst are shown in Fig. 5. As shown in Fig. 5a, the mesoporous structures of 25Ni/MA remain unchanged during reaction, indicating that the reaction of CO_2 methanation does not destroy the mesoporous structures. The elemental mapping shown in Fig. 5b–e presents the existing of Ni, Al and O, respectively. Only metallic Ni element (Fig. 5d) is observed for the marked nanoparticle (red circle in Fig. 5b) on the surface layers, whereas no Al or O exists (Fig. 5c and e), indicating that the NiO phase on the surface of 25Ni/MA has been converted completely to metallic Ni in the CO_2 methanation reaction. The spent Ni nanoparticles size is about 25 nm, indicating that the Ni particles remain a stable state, and no sintering of Ni nanoparticles appeared during reaction. This might be attributed to the fabric-like walls of MA, suppressing the aggregation of Ni nanoparticles during the reaction.

3.2 Catalyst testing

CO_2 methanation performances of the Ni/MA catalysts are shown in Fig. 6. As shown in Fig. 6a, the catalytic activity of all of the catalysts increases firstly with the increasing reaction temperature, and then reaches the maximum value at a specified temperature. Subsequently, the catalytic activity begins to

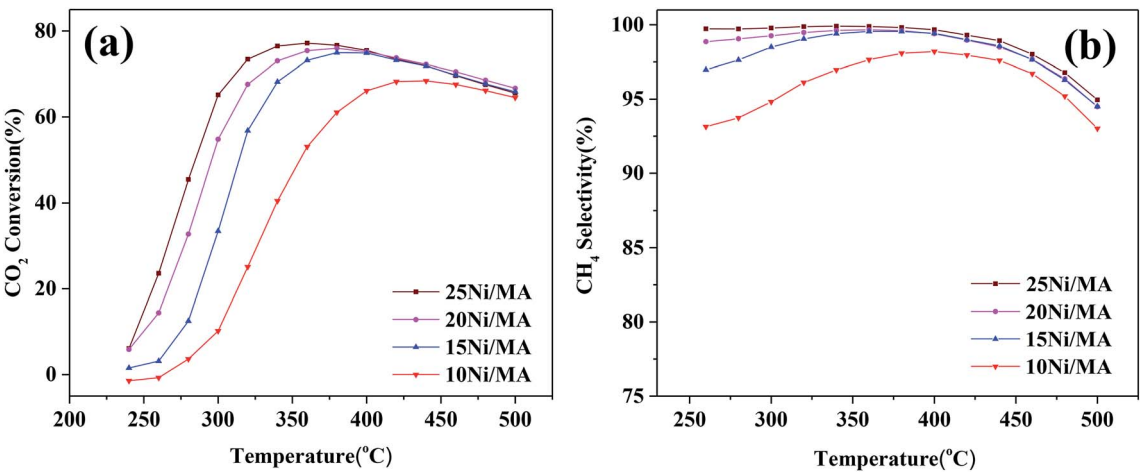

Fig. 6 (a) CO_2 conversion and (b) CH_4 selectivity of Ni/MA catalysts, GHSV = 6000 mL g^{-1} h^{-1}, H_2/CO_2 = 4, 1 atm.

Open Access Article. Published on 15 March 2019. Downloaded on 11/6/2025 12:59:15 AM.
This article is licensed under a Creative Commons Attribution-NonCommercial 3.0 Unported Licence.

decrease with further increasing temperature. A similar changing trend is observed for CH_4 selectivity (Fig. 6b). The maximum value (77.2% of CO_2 conversion and 99.9% of CH_4 selectivity) is displayed at 360 °C over the 25Ni/MA catalyst. When the temperature is higher than 360 °C, CO_2 conversion and CH_4 selectivity begin to drop. As we known, CO_2 methanation is an exothermic reaction, which is favorable at low temperature based on its thermodynamic equilibrium.[40] Raising the reaction temperature facilitates the reverse water-gas shift reaction, increasing the amount of CO vice-product.

The effect of nickel loadings on the catalytic performances is further studied. From Fig. 6a it can be found that CO_2 conversion presents an increasing trend with the increasing Ni content. The optimal catalytic activity increases from 62 to 77% as the Ni content increases from 10 to 25%, accompanied with the obvious decrease of suitable reaction temperature from 420 to 360 °C. It is generally accepted that metallic Ni plays a unique role in providing active sites for CO_2 methanation. Rahmani *et al.*[35] prepared the Ni/Al_2O_3 catalysts with different Ni loadings, and found that CO_2 conversion increased gradually with the increasing nickel loading in CO_2 methanation. Du *et al.*[26] investigated CO_2 methanation performance of Ni-MCM-41 catalysts containing 1–3 wt% Ni species, and found that higher selectivity and space-time yield were obtained for the Ni-MCM-41 catalyst with higher Ni loading. In the present study, Ni species added into the MA support is dispersed well on the MA support without entering into the mesoporous structures, confirmed by the BET, SEM and TEM results. In addition, the H_2-TPR results indicate that the amount of α-type and β-type Ni species increases with the Ni loading increasing, implying that incorporation of more Ni species into MA weakens the metal–support interaction, promoting the reduction of NiO and increasing the amount of active metallic Ni sites, which plays a critical role in improving the CO_2 methanation performance.[7] The used Ni/MA catalyst with higher Ni loading presents more active metallic Ni sites confirmed also by both the XRD and XPS results, which further provides more active sites for CO_2 methanation. Especially, the adding of more Ni loading increases the particles size of NiO, as confirmed by XRD, which facilitates the weakened interaction of Ni–MA, promoting the formation of active metallic Ni. It is also considered that the particle size of NiO plays an indirect role in promoting the catalytic activity.

On the other hand, it is seen that the CH_4 selectivity in the range of 250–400 °C increases gradually with the increasing in nickel loading (shown in Fig. 6b). As the reaction temperature is over 400 °C, CH_4 selectivity for all of the catalysts begins to decrease with the increasing temperature on stream, which may be attributed to the reverse water gas shift reaction,[26] resulting in the conversion of CO_2 to CO, decreasing the CH_4 selectivity.

In addition, comparison of CO_2 methanation performance for MA modified and CA modified Ni catalysts are shown in Fig. 7. It can be found that the MA modified Ni catalyst presents higher catalytic activity and CH_4 selectivity compared to the traditional CA modified Ni catalyst. The optimal CO_2 conversion of 25Ni/CA is 73.6% at 380 °C, whereas that of 25Ni/MA is 77.2% at 360 °C, revealing better low-temperature CO_2 methanation activity by the modification of MA (Fig. 7a). According to the N_2 adsorption–desorption analysis and XRD results mentioned above, the MA support prepared by partial hydrolysis method displays BET surface area of 237 $m^2\ g^{-1}$ and average pore size of 3.1 nm. The commercial CA presents a lower BET surface area about 1.4 times (166 $m^2\ g^{-1}$) and a higher pore size about 1.5 times (4.7 nm). Therefore, larger surface area and narrower pore size of MA facilitate the dispersion of active nickel species on the surface, promoting the catalytic activity at lower temperature.

In order to further analyze the effect of other Al_2O_3 support with different pore size on the CO_2 methanation performance, the results of Rahmani *et al.*[41] have been selected herein. Comparative data are listed in Table 1S (in the ESI†). From Table 1S† it can be found that the Al_2O_3 support is prepared by sol–gel method, which exhibits higher pore size of 8.1 nm

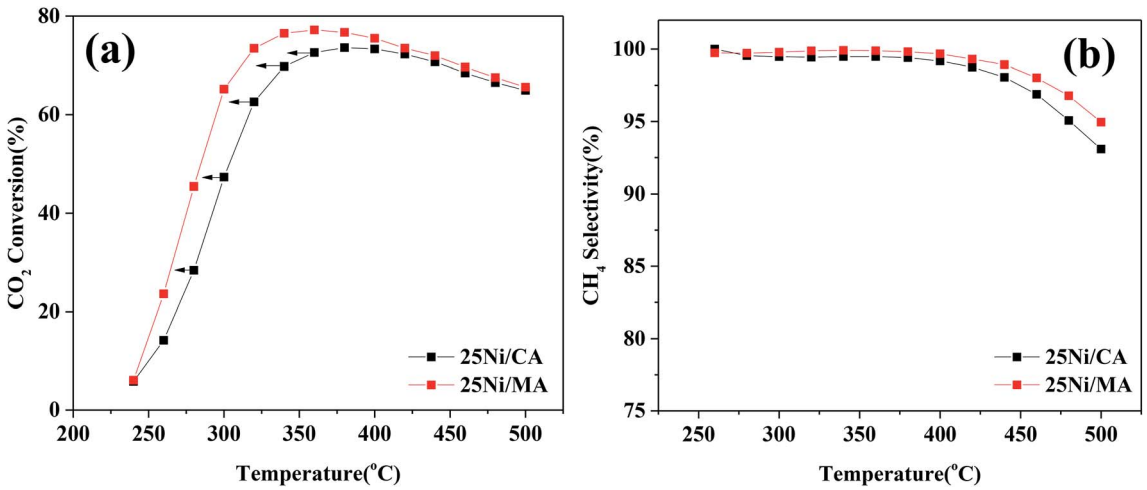

Fig. 7 (a) CO_2 conversion and (b) CH_4 selectivity of 25Ni/CA and 25Ni/MA catalysts, GHSV = 6000 mL g^{-1} h^{-1}, H_2/CO_2 = 4, 1 atm.

Open Access Article. Published on 15 March 2019. Downloaded on 11/6/2025 12:59:15 AM.
This article is licensed under a Creative Commons Attribution-NonCommercial 3.0 Unported Licence.

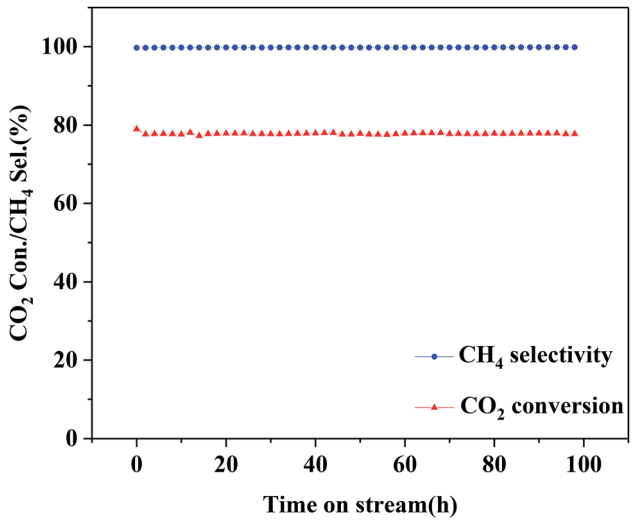

Fig. 8 Stability test of the 25Ni/MA catalyst at 340 °C, GHSV = 6000 mL g^{-1} h^{-1}, H_2/CO_2 = 4, 1 atm.

compared to the MA support in the present study. However, the optimized CO_2 conversion for 25Ni/Al_2O_3 reported by Rahmani *et al.*[41] is 73% at 350 °C, which is lower than the value of 25Ni/MA in this study, suggesting that the MA support with narrower pore size by partial hydrolysis preparation method displays an outstanding CO_2 methanation performance. In addition, some typical Ni-based catalysts for CO_2 methanation are selected. From Table 2S† it is seen that the Ni/MA catalyst presents the highest CO_2 conversion at a low temperature, further verifying excellent CO_2 methanation performance of the MA support modified Ni catalyst.

The optimized 25Ni/MA catalyst is carried out for the stability test. As shown in Fig. 8, the 25Ni/MA catalyst presents 77% of catalytic activity with almost 100% of CH_4 selectivity, which remains unchanged during the reaction for 100 h, indicating that modification by the MA support improves obviously the catalyst stability. Furthermore, higher temperature methanation (400 °C) of MA and CA supported Ni catalysts is tested (Fig. 1S†). From Fig. 1Sa† it can be seen that the Ni/MA catalyst displays the excellent stability in 400 °C, and there is no deactivation appeared during reaction. In contrast, the catalytic activity of the Ni/CA catalyst decreases gradually in the initial stage and then remained unchanged basically with time on stream. Especially, the CH_4 selectivity begins to decrease after reaction for 27 h (Fig. 1Sb†). Besides, the reusability of 25Ni/MA at 400 °C is further tested (Fig. 2S†), and no deactivation of the catalyst is observed during reaction for 80 h. All of these results suggest that the CA supported Ni catalyst takes place easily the deactivation in the CO_2 methanation reaction, while the MA support plays a critical role in improving the stability of the catalyst.

The TEM results indicate that metallic Ni is formed on the surface of MA. No aggregation of Ni particles and no formation of carbon deposition are exhibited. It is possible that the MA support with cross-linked fabricate walls restrains the aggregation of metallic Ni particles, improving the catalyst stability. The micro-structures of the spent catalyst are further analyzed. The spent 25Ni/MA catalyst after reaction for 100 h is characterized by XRD. From Fig. 9a it is seen that phase composition of the spent 25Ni/MA is composed mainly of metallic Ni. The Ni particle size calculated using Scherrer equation is about 21.5 nm, which is close to the value in initial reaction, further validating the stability of Ni active nanoparticles during the CO_2 methanation process.

The behavior of carbon deposition over the Ni/MA catalysts is analyzed by TG. As shown in Fig. 9b, two weight loss steps can be seen for all of the spent catalysts. The first weight loss in zone I (below 290 °C) is attributed to thermal desorption of physical adsorbed H_2O, and the second weight loss in zone III (above 420 °C) is related to the removal of graphite coke that led to the catalyst deactivation.[42,43] Besides, there is a weight gain in zone II (290–420 °C) for the 20Ni/MA and 25Ni/MA catalysts, which is ascribed to the oxidation of reduced Ni species.[44] It is possible that more metallic Ni sites formed over the spent Ni/MA catalyst with higher Ni loading facilitate the oxidation of metallic Ni. From Fig. 9b, it is seen that all catalysts display excellent carbon resistance with only 2.8% carbon

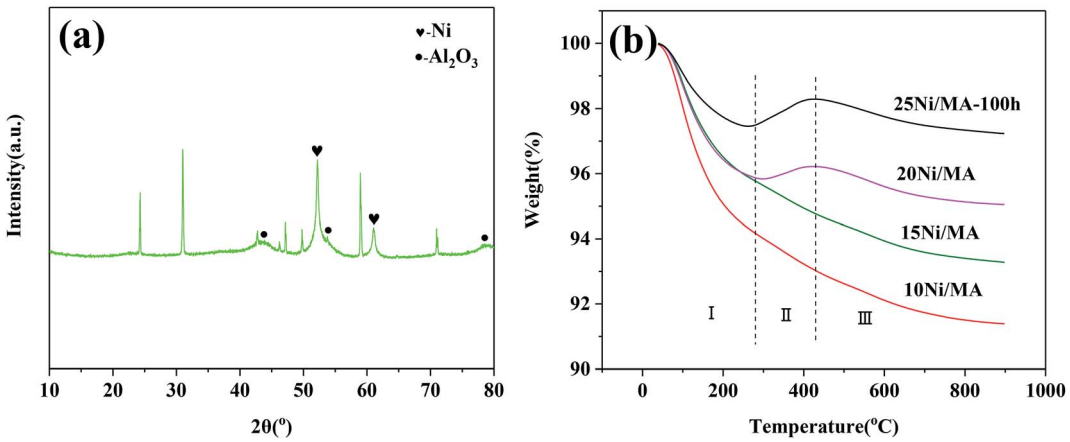

Fig. 9 (a) XRD pattern of the 25Ni/MA catalyst after 100 h reaction and (b) TG curves of the spent Ni/MA catalysts.

Open Access Article. Published on 15 March 2019. Downloaded on 11/6/2025 12:59:15 AM.
This article is licensed under a Creative Commons Attribution-NonCommercial 3.0 Unported Licence.

deposition amount at most. The weight loss of the used 25Ni/MA catalyst (100 h) is only 1.1%, revealing excellent anti-coking ability. This is consistent with the TEM results mentioned above.

4 Conclusions

In summary, the Ni/MA catalysts with different Ni loadings were facilely prepared using partial hydrolysis using inorganic aluminum salt and employed for CO_2 methanation. The MA modified Ni catalyst displayed higher catalytic activity and CH_4 selectivity as well as excellent stability compared to the traditional Ni/CA catalyst. The characterization results indicated that the MA support was synthesized successfully by partial hydrolysis method, and displayed excellent hydrothermal stability. Modification of MA decreased the metal–support interaction, promoting the reduction of NiO species and formation of metallic Ni active sites over the Ni/MA catalysts. The monolithic skeleton of MA with fabric-like walls stabilized the nano-nickel particle sizes, which restrained the sintering of metallic Ni particles and carbon deposition on the catalyst, promoting obviously the catalyst stability.

Conflicts of interest

There are no conflicts to declare.

Acknowledgements

The authors gratefully acknowledge the financial support from International cooperation and exchange program of the National Natural Science Foundation of China (51861145102), International Science and Technology cooperation project of Xinjiang Production and Construction Corps (2017BC008), 111 project (B12015) and Fundamental Research Fund for the Central Universities (2042017kf0173).

References

1 M. Streibel, N. Nakaten, T. Kempka and M. Kühn, *Energy Procedia*, 2013, **40**, 202–211.
2 J. Kopyscinski, T. J. Schildhauer and S. M. A. Biollaz, *Fuel*, 2010, **89**, 1763–1783.
3 M. Aresta and A. Dibenedetto, *Dalton Trans.*, 2007, **28**, 2975–2992.
4 T. Abe, M. Tanizawa, K. Watanabe and A. Taguchi, *Energy Environ. Sci.*, 2009, **2**, 315–321.
5 J. Liu, W. Bing, X. Xue, F. Wang, B. Wang, S. He, Y. Zhang and M. Wei, *Catal. Sci. Technol.*, 2016, **6**, 3976–3983.
6 A. H. Zamani, R. Ali and W. A. W. A. Bakar, *J. Taiwan Inst. Chem. Eng.*, 2014, **45**, 143–152.
7 M. Younas, L. Loong Kong, M. J. K. Bashir, H. Nadeem, A. Shehzad and S. Sethupathi, *Energy Fuels*, 2016, **30**, 8815–8831.
8 T. A. Le, M. S. Kim, S. H. Lee, T. W. Kim and E. D. Park, *Catal. Today*, 2017, **293–294**, 89–96.
9 G. Zhou, H. Liu, K. Cui, H. Xie, Z. Jiao, G. Zhang, K. Xiong and X. Zheng, *Int. J. Hydrogen Energy*, 2017, **42**, 16108–16117.
10 Y. Yan, Y. Dai, H. He, Y. Yu and Y. Yang, *Appl. Catal., B*, 2016, **196**, 108–116.
11 I. Ganesh, *Renewable Sustainable Energy Rev.*, 2014, **31**, 221–257.
12 S. Rönsch, J. Schneider, S. Matthischke, M. Schlüter, M. Götz, J. Lefebvre, P. Prabhakaran and S. Bajohr, *Fuel*, 2016, **166**, 276–296.
13 C. Song, *Catal. Today*, 2006, **115**, 2–32.
14 J. Gao, Q. Liu, F. Gu, B. Liu, Z. Zhong and F. Su, *RSC Adv.*, 2015, **5**, 22759–22776.
15 J. N. Park and E. W. McFarland, *J. Catal.*, 2009, **266**, 92–97.
16 Y. Feng, W. Yang and W. Chu, *Integr. Ferroelectr.*, 2016, **172**, 40–48.
17 G. Zhi, X. Guo, X. Guo, Y. Wang and G. Jin, *Catal. Commun.*, 2011, **16**, 56–59.
18 H. C. Wu, Y. C. Chang, J. H. Wu, J. H. Lin, I. K. Lin and C. S. Chen, *Catal. Sci. Technol.*, 2015, **5**, 4154–4163.
19 F. Song, Q. Zhong, Y. Yu, M. Shi, Y. Wu, J. Hu and Y. Song, *Int. J. Hydrogen Energy*, 2017, **42**, 4174–4183.
20 K. Zhao, W. Wang and Z. Li, *J. CO2 Util.*, 2016, **16**, 236–244.
21 G. Zhou, H. Liu, K. Cui, A. Jia, G. Hu, Z. Jiao, Y. Liu and X. Zhang, *Appl. Surf. Sci.*, 2016, **383**, 248–252.
22 S. Tada, T. Shimizu, H. Kameyama, T. Haneda and R. Kikuchi, *Int. J. Hydrogen Energy*, 2012, **37**, 5527–5531.
23 S. Tada, D. Minori, F. Otsuka, R. Kikuchi, K. Osada, K. Akiyama and S. Satokawa, *Fuel*, 2014, **129**, 219–224.
24 M. C. Bacariza, I. Graça, S. S. Bebiano, J. M. Lopes and C. Henriques, *Chem. Eng. Sci.*, 2018, **175**, 72–83.
25 R. Merkache, I. Fechete, M. Maamache, M. Bernard, P. Turek, K. Al-Dalama and F. Garin, *Appl. Catal., A*, 2015, **504**, 672–681.
26 G. Du, S. Lim, Y. Yang, C. Wang, L. Pfefferle and G. L. Haller, *J. Catal.*, 2007, **249**, 370–379.
27 S. A. Hassanzadeh-Tabrizi and E. Taheri-Nassaj, *Mater. Lett.*, 2009, **63**, 2274–2276.
28 A. Khaleel and B. Dellinger, *Environ. Sci. Technol.*, 2002, **36**, 1620–1624.
29 L. Xu, F. Wang, M. Chen, H. Yang, D. Nie, L. Qi and X. Lian, *RSC Adv.*, 2017, **7**, 18199–18210.
30 X. Shang, X. Wang, W. Nie, X. Guo, X. Zou, W. Ding and X. Lu, *J. Mater. Chem.*, 2012, **22**, 23806–23814.
31 L. Xu, F. Wang, M. Chen, J. Zhang, K. Yuan, L. Wang, K. Wu, G. Xu and W. Chen, *RSC Adv.*, 2016, **6**, 28489–28499.
32 A. Zhao, W. Ying, H. Zhang, H. Ma and D. Fang, *Catal. Commun.*, 2012, **17**, 34–38.
33 J. Zhang, H. Xu, X. Jin, Q. Ge and W. Li, *Appl. Catal., A*, 2005, **290**, 87–96.
34 M. Cai, J. Wen, W. Chu, X. Cheng and Z. Li, *J. Nat. Gas Chem.*, 2011, **20**, 318–324.
35 S. Rahmani, M. Rezaei and F. Meshkani, *J. Ind. Eng. Chem.*, 2014, **20**, 4176–4182.
36 M. Lenglet, A. D'huysser, J. P. Bonelle, J. Dürr and C. K. Jørgensen, *Chem. Phys. Lett.*, 1987, **136**, 478–482.
37 N. S. Mcintyre and M. G. Cook, *Anal. Chem.*, 1975, **47**, 2208–2213.

Open Access Article. Published on 15 March 2019. Downloaded on 11/6/2025 12:59:15 AM.
This article is licensed under a Creative Commons Attribution-NonCommercial 3.0 Unported Licence.

38 J. Liu, C. Li, F. Wang, S. He, H. Chen, Y. Zhao, M. Wei, D. G. Evans and X. Duan, *Catal. Sci. Technol.*, 2013, **3**, 2627–2633.
39 Y. Li, G. Lu and J. Ma, *RSC Adv.*, 2014, **4**, 17420–17428.
40 L. Zhou, Q. Wang, L. Ma, J. Chen, J. Ma and Z. Zi, *Catal. Lett.*, 2015, **145**, 612–619.
41 S. Rahmani, M. Rezaei and F. Meshkani, *J. Ind. Eng. Chem.*, 2014, **20**, 1346–1352.
42 A. I. Tsyganok, T. Tsunoda, S. Hamakawa, K. Suzuki, K. Takehira and T. Hayakawa, *J. Catal.*, 2003, **213**, 191–203.
43 Z. Xu, M. Zhen, Y. Bi and K. Zhen, *Appl. Catal., A*, 2000, **198**, 267–273.
44 D. Liu, R. Lau, A. Borgna and Y. Yang, *Appl. Catal., A*, 2009, **358**, 110–118.

 This journal is © The Royal Society of Chemistry 2019